Tracking structure and composition changes in oxide derived Cu-Sn catalysts during CO₂ electroreduction using X-ray spectroscopy

Laura C. Pardo Pérez,[a] Alexander Arndt,[a,b] Sasho Stojkovikj,[a,b] Ibbi Y. Ahmet,[c] Veronica Davies,[a,b] Katja Höflich,[c†] Eike Köhnen,[d] Philipp Tockhorn,[d] Ronny Golnak,[e] Jie Xiao,[e] Götz Schuck [f] and Matthew T. Mayer*[a]

In the field of electrochemical CO_2 conversion, the development of earth-abundant catalysts which are selective for a single product is a central challenge. Cu-Sn bimetallic catalysts have been reported to yield selective CO_2 reduction towards either carbon monoxide or formate. To advance the understanding of possible synergetic effects between Cu and Sn which direct product selectivity, a thorough investigation of the catalyst structure and composition in its active state is desired. We present an X-ray spectroscopy investigation of oxide-derived Cu-Sn catalysts prepared by functionalization of $Cu(OH)_2$ nanowire arrays with ultrathin SnO_2 overlayers. This method allows precisely tunable Sn composition, which enables synthesis of composite catalysts with high selectivity toward either CO or formate. Under CO_2 reduction conditions, the materials undergo significant transformations before reaching their catalytically active forms. Complementary information on the electrocatalysts' dynamic bulk and surface structure was revealed via correlating observations from multiple X-ray spectroscopy methods. *In situ* investigations of Cu K-edge revealed that in the bulk Cu is fully reduced from Cu^{2+} to Cu° after a pre reduction step. *Quasi in situ* XPS demonstrated that, at the catalyst surface, Cu is also present exclusively as Cu°, whereas significant differences in Sn quantification and speciation were observed between the CO- and formate-selective catalysts. After CO_2 electrolysis, CO-selective catalysts exhibited a surface Sn content of 13 at. % predominantly present as Sn oxide, while the formate-selective catalysts had a Sn content of ~70 at. % consisting of both metallic Sn° and Sn oxide species. Our study reveals the complex dependence of catalyst structure, composition, and speciation with applied electrochemical bias in Sn-functionalized nanostructured Cu catalysts.

Broader context

The extraction and consumption of fossil-derived carbon is causing a dangerous imbalance in atmospheric carbon dioxide (CO_2) levels, resulting in climate change which threatens human survival. Clearly, the unsustainable use of fossil carbon must be stopped as soon as possible, but this will require a massive technological shift which includes finding alternative, sustainable routes for producing the important carbon-based chemicals and fuels on which society depends. A promising approach is to treat CO_2 not simply as waste, but rather as a resource. By capturing CO_2 at point sources, or extracting it directly from air, CO_2 can be a carbon-neutral feedstock for sustainable production of chemicals and fuels, while simultaneously helping to mitigate further emissions. Converting CO_2 into more valuable molecules requires significant energy input and can produce a variety of different small-molecule products, usually as an undesirable mixture. Driving this process with renewable electricity – via electrochemistry – is an attractive approach, but designing an electrochemical process capable of selectively producing just one desired product is an important challenge, one that is being addressed by innovative design of new catalyst materials.

[a.] *Young Investigator Group Electrochemical Conversion of CO_2, Helmholtz-Zentrum Berlin für Materialien und Energie GmbH, Hahn-Meitner-Platz 1, 14109 Berlin, Germany*
 * E-mail: m.mayer@helmholtz-berlin.de
[b.] *Institut für Chemie & Biochemie, Freie Universität Berlin, 14195 Berlin, Germany*
[c.] *Institute for Solar Fuels, Helmholtz-Zentrum Berlin für Materialien und Energie GmbH, Hahn-Meitner-Platz 1, 14109 Berlin, Germany*
[d.] *Young Investigator Group Perovskite Tandem Solar Cells, Helmholtz-Zentrum Berlin für Materialien und Energie GmbH, Kekuléstraße 5, 12489 Berlin, Germany*
[e.] *Department Highly Sensitive X-ray Spectroscopy, Helmholtz-Zentrum Berlin für Materialien und Energie GmbH, Albert-Einstein-Straße 15, 12489 Berlin, Germany*
[f.] *Department Structure and Dynamics of Energy Materials, Helmholtz-Zentrum Berlin für Materialien und Energie GmbH, Hahn-Meitner-Platz 1, 14109 Berlin, Germany*
† present address: Ferdinand-Braun-Institut gGmbH, Leibniz-Institut für Höchstfrequenztechnik, 12489 Berlin, Germany

Introduction

Copper-based electrocatalysts have been widely studied for CO_2 electrochemical reduction (CO₂ER) due to their unique capability to produce valuable products such as CO, hydrocarbons, and alcohols. As many as 16 products have been observed during CO₂ER on polycrystalline Cu.[1] The typical major products are formate, CO, ethylene and methane, minor products include alcohols and other oxygenates and H_2 is a common (often predominant) side product from the hydrogen evolution reaction (HER). Directing selectivity among this wide variety of products remains a pressing challenge in the field.[2] Diverse catalyst engineering approaches to improve the selectivity of Cu have been advanced in the field including the use of nanostructured[3–6] as well as oxide derived Cu catalysts,[7–]

[12] as discussed in the comprehensive review by Nitopi et al.[13] Another possible approach to modulate Cu selectivity is to functionalize the Cu surfaces with a second metal to form Cu-M bimetallic catalysts.[14,15] In particular, several studies on the CO_2ER activity of Cu-Sn catalysts have demonstrated remarkably high selectivity towards CO[16,17] or formate[18,19]. Although a number of empirical trends correlating composition and structure with observed selectivity have been reported, the precise mechanistic effects directing selectivity remain a topic of some debate.

Comparison of several studies employing various Cu-Sn stoichiometries with similar morphologies[20–22] indicates generally that Cu-Sn catalysts with low Sn content are typically selective towards CO production, while those with high Sn content favor formate ($HCOO^-$). However, specific optimal compositions leading to high activity towards CO or formate vary significantly among reports. Furthermore, improved activity and selectivity are reported in catalysts with high surface area. Highly CO-selective catalysts have been achieved by the functionalization of high surface area Cu nanostructures with low amounts of Sn by electrodeposition,[23,24] electroless deposition[25] or atomic layer deposition (ALD) of SnO_2.[16] Interestingly, high surface area Cu nanostructures functionalized with Sn overlayers have also been reported as highly selective catalysts towards formate.[19,22,26] Presumably, significant differences in Cu-Sn surface structure and composition exist among these high surface area catalysts selective toward different products, but unfortunately the detailed analysis of surface composition is rarely reported. Therefore, an investigation of composition and speciation in Sn-functionalized Cu nanostructures tuned to yield radically different selectivity (namely CO or formate) is of high interest to help unravel the factors which direct this selectivity.

Various explanations of the synergetic effects that yield these high selectivities of Cu-Sn bimetallic catalysts have been proposed. According to DFT investigations, increased HER overpotentials are predicted on Cu-Sn surfaces compared to pure Cu, for both low[17] and high[27] Sn content catalysts, leading to an increased relative selectivity for CO_2ER over HER on Cu-Sn materials. As for the possible effects of Cu-Sn composition directing selectivity among CO or formate pathways, Vasileff[28] reported a Bader charge analysis indicating a partial electron transfer from Sn to Cu in CuSn alloys, leading to the formation of partially oxidized $Sn^{\delta+}$ sites and partially reduced $Cu^{\delta-}$ sites. This partial electron transfer is proposed to gradually weaken the adsorption of *COOH (leading to CO) with increasing Sn content, and enhance *OCHO adsorption (leading to $HCOO^-$). Meanwhile, the persistence of oxidized Sn as active site during CO_2ER experiments has been invoked by Li et al. based on DFT studies,[22] who proposed that Cu-doped uniaxially-compressed SnO_2 is the active site for selective reduction of CO_2 to CO in Cu@SnO_2 (core@shell) nanoparticle catalysts.

These DFT studies on Cu-Sn bimetallic CO_2ER catalysts indicate that charge distribution among metal sites and their oxidation states play a crucial role in the binding strength of the key intermediates directing selectivity between H_2, CO and formate. At the center of the debate is the possible persistence of oxidized metal sites under CO_2ER reduction conditions and the precise nature of the active site. While these DFT models are typically based on compositions observed either before or after electrocatalyst testing, it is well known that electrocatalyst materials can transform significantly under CO_2 reduction conditions, presenting challenges in identifying their actual active forms. In this context, the complementary techniques of X-ray absorption (XAS) and X-ray photoelectron (XPS) spectroscopy are powerful techniques to probe the chemical environment and oxidation state of Cu and Sn and gather relevant information on the active form of the catalysts.

Herein, we present an X-ray spectroscopy study of a Cu-Sn bimetallic system with tunable Sn content capable of achieving high selectivity to either CO or formate. Complementary information on the composition and chemical environment of metals in the electrocatalysts' bulk and surface was revealed by correlating observations from multiple X-ray spectroscopy methods (*in situ* hard-XAS, *ex situ* soft-XAS and *quasi in situ* XPS). Our study reveals a complex dependence of catalyst structure, composition, and speciation with applied electrochemical bias in Sn-functionalized Cu catalysts.

Results & discussion

The preparation of nanostructured Cu-Sn electrocatalysts was adapted from the method reported by Schreier et al.[16] Complete experimental details are provided in the Supplementary Information (ESI S.1). In a first step, electrodes based on arrays of $Cu(OH)_2$ nanowires, denoted hereafter CuNW, were synthesized by anodization of Cu films (1 µm) sputter deposited on glass substrates. The anodization was carried out at a constant current of 8 mA cm^{-2} to reach a total charge of 1.35 C cm^{-2} and the samples were subsequently annealed in air at 150 °C for 1 h (Figure 1a). This procedure yields reproducible bundled nanowire arrays with lengths of several µm (~8-10 µm) and diameters of hundreds of nm (200-400 nm), which are attached to a continuous Cu base layer, as seen in Figures 1b-d.

The so-obtained $Cu(OH)_2$ nanowires were then modified by ultrathin SnO_2 layers generated by atomic layer deposition (ALD) with varied number of deposition cycles, denoted hereafter CuNW-SnXc (Xc = X number of ALD cycles). The ALD method allows uniform and conformal coating of the high surface area nanostructures with SnO_2, and variation of the deposition cycles enables us to precisely modulate the surface Sn content, while avoiding significant changes in morphology (Figure 1 and S1). The number of deposition cycles were varied across the range 1–182, which correspond to expected nominal thicknesses of approximately 0.1–20 nm based on calibrated deposition rates. The XRD patterns of the samples modified with 15 and 182 ALD cycles of SnO_2 display the typical pattern for CuO (Figure 1e), indicating that the $Cu(OH)_2$ nanowires are dehydrated under the ALD conditions (120 °C under vacuum). Note that the observed Cu° metallic diffraction peaks arise from the underlying residual sputtered Cu, as can be seen in the cross-section SEM micrograph (Figure 1d). This continuous Cu layer–a result of only partially anodizing the original film–is
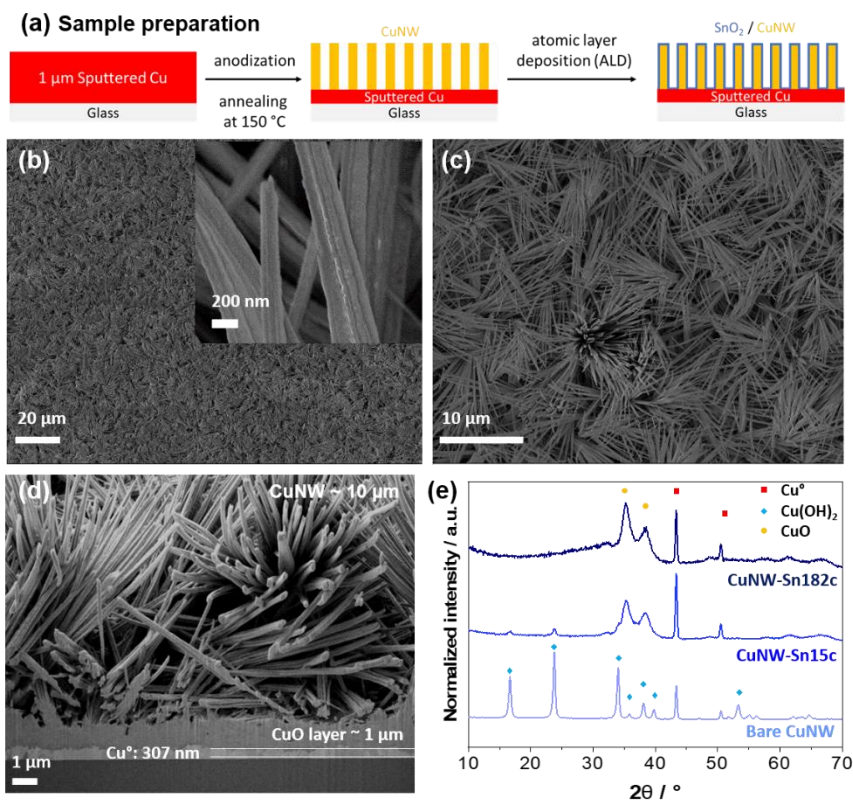
Figure 1. (a) Schematic of synthesis procedure. (b), (c) SEM micrographs of the as-synthesized CuNW modified with 15 cycles of ALD SnO_2. (d) Cross section SEM micrograph of CuNW-Sn-15c at Focused Ion Beam FIB cut. (e) Grazing incidence XRD patterns of as-synthesized CuNW bare and modified with 15 or 182 cycles of SnO_2 ALD.

important for maintaining the integrity and conductivity of the NW arrays as a functioning electrode.

The samples were tested for CO_2 electroreduction in CO_2 saturated 0.1 M $KHCO_3$ in a custom made three-electrode two-compartment cell separated by a Nafion 115 membrane, under constant flow of CO_2. Since the CuNW-SnXc were originally composed of $Cu(OH)_2$ (bare CuNW) or CuO (SnO_2 ALD modified samples) and variable amounts of SnO_2, the oxide composites were pre-reduced by chronopotentiometry (CP) at constant current of -2 mA cm^{-2} to reach a potential of -0.5 V vs RHE (all potentials reported hereafter are referred to RHE unless otherwise specified). Directly after the pre-reduction step, the samples were set at the desired CO_2ER electrolysis potential, typically -0.7 V where the maximum efficiency for CO has been reported for this system.[16] Representative pre-reduction CP and chronoamperometry data are presented in ESI Figure S2. The CO_2ER activity at -0.7 V for samples modified with various numbers of SnO_2 ALD cycles (between 1–182) is displayed as faradaic efficiency and partial current densities in Figure 2a and 2b, respectively. The results show that modifying the CuNW with a single cycle of SnO_2 induces a significant shift in selectivity, namely the near-complete suppression of formate and a large increase in CO selectivity. Increasing the SnO_2 to 15 cycles further improves CO selectivity over H_2 and ethylene, reaching an optimal faradaic efficiency together with the highest CO partial current density (Figure 2b). Further increasing SnO_2 to 20, 25, and 182 cycles (~20 nm) induces a decrease in CO selectivity and production rate, as well as total current density. Such volcano-type behavior was previously

reported by Schreier et al.[16] albeit with different optimal number of SnO_2 ALD cycles, presumably due to the use of different ALD system conditions. As noted above, the $Cu(OH)_2$ dehydrates to CuO during the ALD process. We performed a series of control experiments, pre-dehydrating $Cu(OH)_2$ to CuO before ALD (ESI Figure S3). The results indicate that the dehydration of $Cu(OH)_2$ to CuO itself induces only minor changes in CO_2ER selectivity, whereas after addition of 15 ALD cycles of SnO_2 to each, the Sn-functionalized $Cu(OH)_2$ and CuO nanowire samples both obtained high CO faradaic efficiency (79% and 83% respectively).

The CuNW modified with 15 ALD cycles, hereafter denoted CuNW-Sn$_{LOW}$, displays the optimal composition for CO production with the highest faradaic selectivity (79%) and CO partial current density of ~- 2.5 mA cm^{-2}. Its CO_2ER performance was further investigated in the potential range from -0.5 to -0.9 V (Figure 2c). This composite displays high CO selectivity across the moderate overpotential range -0.6 to -0.8 V, decreasing at lower and higher potentials in favor of increased hydrogen evolution. Low formate selectivity is observed across the examined range. Therefore, this addition of an ultrathin ALD layer of SnO_2 (15 cycles correspond to a nominal thickness ~1.6 nm) results in a significant alteration of product selectivity toward CO, as compared to the mixture of several products observed on bare CuNW (CO_2ER activity shown in ESI Figure S4). The observation that this intermediate loading of SnO_2 produced the best selectivity and rate for CO formation suggests that there is an important synergy between Cu and Sn which is responsible for this optimized activity.
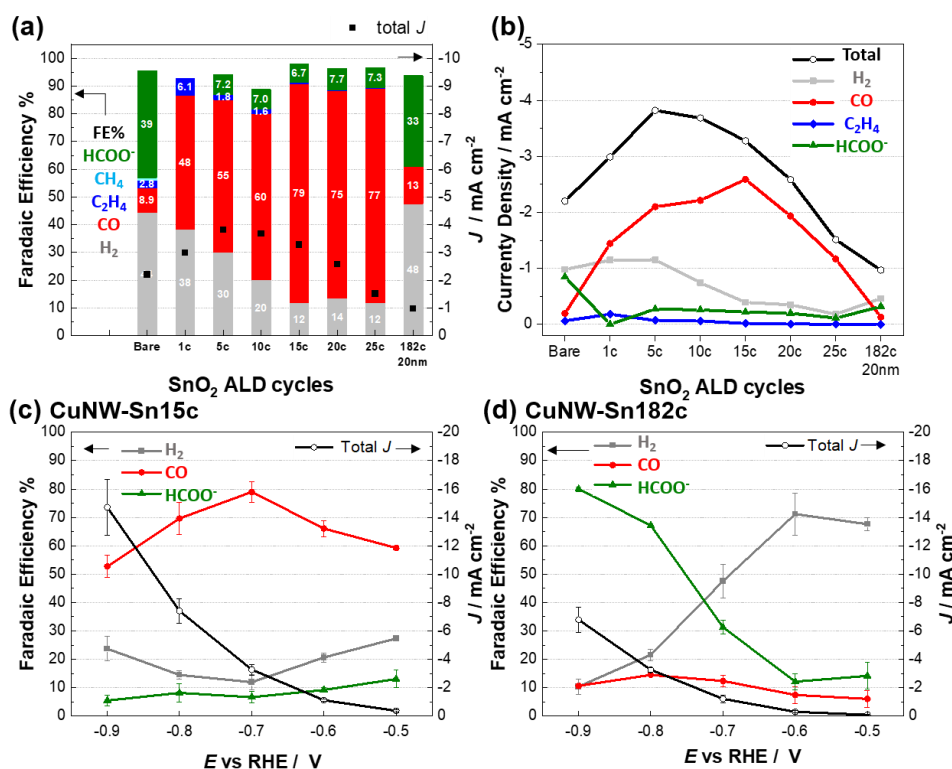
3

Figure 2. CO_2ER activity for different CuNW samples modified with various numbers of SnO_2 ALD cycles, each tested at -0.7 V vs RHE in 0.1 M $KHCO_3$. (a) Faradaic efficiencies and (b) partial current densities. CO_2ER as a function of applied potential for (c) CuNW-Sn15c and (d) CuNW-Sn182c. Error bars correspond to standard deviation of at least three independent samples tested at each potential.

The CuNW modified with a high SnO_2 content (182 ALD cycles, corresponding to a nominal film thickness of approx. 20 nm), hereafter denoted CuNW-Sn_{HIGH}, was also investigated across the same potential range (Figure 2d). Although at -0.7 V this catalyst produced a mix of products dominated by H_2, at more negative potentials the selectivity to hydrogen greatly decreases while formate increases significantly to become the primary product (FE 80% at -0.9 V). Meanwhile, the CO selectivity for this composite remains low at all tested potentials. Thus, at sufficiently high loading of Sn, the composite samples exhibit high formate selectivity comparable to what has been reported for pure Sn catalysts.[29–31]

Scanning electron microscopy (SEM) characterization of the catalysts after CO_2ER electrolysis is presented in ESI Figure S5. The materials display mostly preserved nanowire structure with roughened surfaces. Energy-dispersive X-ray spectroscopy (EDX) quantification of bulk composition (Table 1, ESI Figure S6 and S7) shows that a decreased Sn content is observed after electrolysis experiments; in CuNW-Sn_{LOW} the bulk Sn fraction (referred to total metal Sn+Cu) decreases from 2.2 ± 0.3 at. % in the as-synthesized catalyst to 1.7 ± 0.1 at. % after electrolysis at -0.9 V. In the case of CuNW-Sn_{HIGH} the Sn content decreases from 23 ± 1.1 at. % in the as-synthesized catalyst to 16 ± 1.3 at. % after electrolysis at -0.9 V. Partial dissolution of Sn was further confirmed by ICP-OES analysis of electrolyte (ESI Table S1).

Together these results demonstrate that the SnO_2 ALD modification of CuNW electrodes enables the modulation of the Cu-Sn bimetallic composition to reach high selectivity toward either CO in CuNW-Sn_{LOW} or formate in CuNW-Sn_{HIGH} with minor

changes to the nanoscale morphology of the electrodes (ESI Figure S1 and section S.5).

These two composites were selected as CO- and formate-selective Cu-Sn catalysts for further investigation of synergetic effects between metals through correlation of observations gathered by different X-ray spectroscopy methods (in situ hard-XAS, ex situ soft-XAS and quasi in situ XPS). Complimentary information on oxidation states and chemical environment of Cu and Sn in CuNW-Sn electrocatalysts' bulk and surface following progressive electroreduction stages has been assessed in order to gather relevant information on the active form of the catalysts. The X-ray spectroscopy observations and their correlation with CO_2ER activity trends are discussed in the following sections.

In situ investigation of Cu K-edge during CO_2ER via hard X-ray absorption spectroscopy

The Cu K-edge XAS measurements were conducted at the KMC-2 beamline at BESSY II.[32] The penetration length of X-ray photons through matter is a function of their energy and the phases though which they pass, with higher energy photons capable of traveling further through condensed matter without complete attenuation. This enables the use of high energy "hard" X-rays for in situ studies of electrode materials in operating electrochemical cells. Photons with energy corresponding to the Cu K-edge (located at 8979 eV) have an approximate probing depth of ~4 μm in Cu and ~1.4 mm in

(a) Cu K-edge XANES

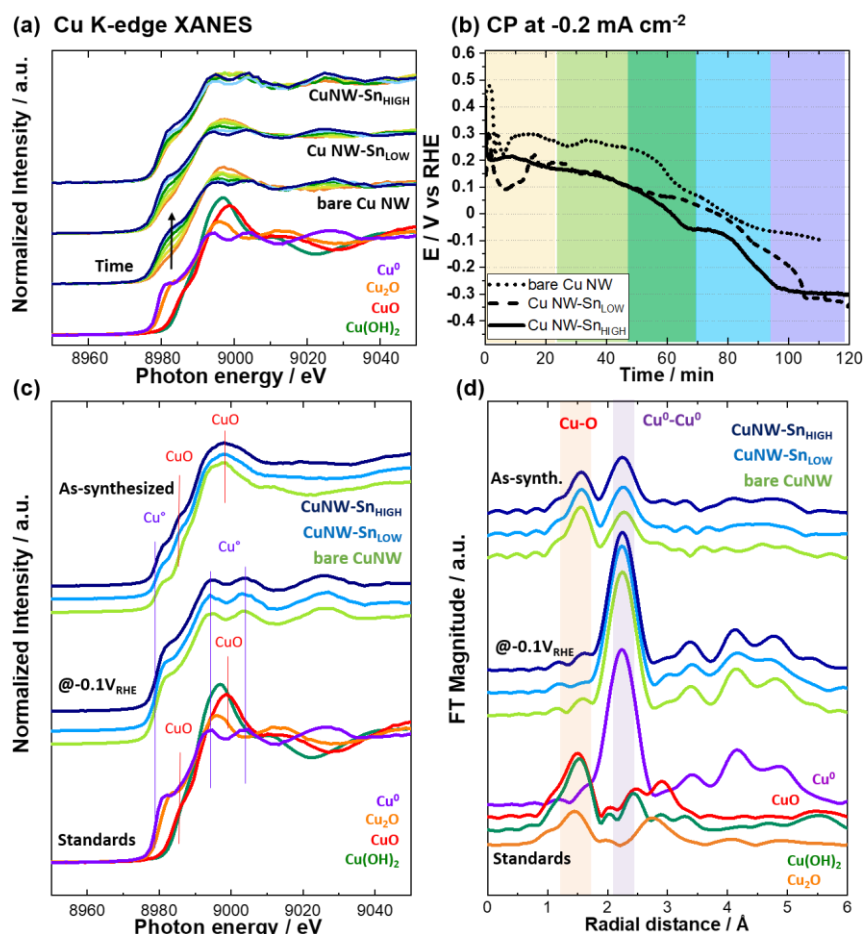**(b) CP at -0.2 mA cm⁻²**

(c)

(d)

Figure 3. In situ Cu K-edge X-ray absorption spectroscopy investigation of CuNW electrodes modified with variable number of SnO₂ ALD cycles. (a) XANES spectra collected during CP activation, (b) CP activation at -0.2 mA cm⁻². The spectra in (a) are color-coded to match the chronopotentiometry time frame (b) in which they were collected. Cu K-edge spectra, (c) XANES and (d) EXAFS, collected in the as-synthesized state and during CO₂ER electrolysis at -0.1 V. Reference spectra collected from standards of metallic Cu°, CuO, Cu(OH)₂ and Cu₂O are presented for comparison.

water.[33,34] A custom electrochemical cell with a polymer window and a thin electrolyte layer of ~500 µm (CO₂ sat. 0.1 M KHCO₃) was fabricated to enable hard X-ray absorption measurements of the electrode in fluorescence detection mode, under electrochemical CO₂ER conditions. The cell and spectroscopy setup employed for these measurements are shown in ESI Figure S9. Considering that the CuNW arrays atop the glass substrate exhibit a porous structure with thickness in the µm range (see Figure 1 b-d), it is expected that the incoming radiation probes the bulk of CuNW and the underlying sputtered Cu as well, as will be discussed later. According to FIB cross-section images the samples have an underlying sputtered Cu° layer of 300-400 nm thickness (Figure 1d and S1).

The CuNW samples modified with different amounts of SnO₂ were investigated in their as-synthesized state as well as *in situ* during both the CP pre-reduction step and CO₂ electrolysis. The Cu K-edge spectra are shown in Figure 3. In the as-synthesized state the bare CuNW electrode displays a spectrum typical of Cu(OH)₂ (Figure 3c). In samples CuNW-Sn_LOW and CuNW-Sn_HIGH the spectra resemble the standard CuO spectrum as indicated by the shoulder ~8982 eV, presumably due to dehydration of Cu(OH)₂ to CuO under ALD conditions (120 °C under vacuum, see experimental details in the Supp. Info.) in agreement with the diffraction patterns (Figure 1e). Additionally, all as-

synthesized samples exhibit an early shoulder at ~8977 eV attributable to the sputtered metallic Cu° layer below the CuNW (Figure 1d). In the EXAFS analysis of as-synthesized samples (Figure 3d) the peak 1.6 Å corresponds to the Cu-O distance in both CuO and Cu(OH)₂, while the peak at 2.3 Å corresponds to the Cu-Cu distance in the underlying sputtered metallic Cu layer, in agreement with previous reports.[35,36]

With the aim of investigating possible effects of Sn content on the progressive reduction of Cu, several Cu K-edge XANES spectra (each acquired for ~20 min) were collected during chronopotentiometric (CP) pre-reduction of bare CuNW as well as samples CuNW-Sn_LOW and CuNW-Sn_HIGH. Although under standard conditions this pre-reduction step was typically carried out at -2 mA cm⁻², taking on average 8-10 min (see ESI Figure S2), here the activation was carried out at lower current density of -0.2 mA cm⁻² in order to allow sufficient time to collect a series of XANES spectra at different stages during the activation step. These spectra are shown in Figure 3a, color-coded to match the chronopotentiometry time frame in which they were collected (Figure 3b). For all types of samples, with or without Sn deposited, the experiments show the progressive transition from Cu²⁺ to Cu° that completes after about 70 min of
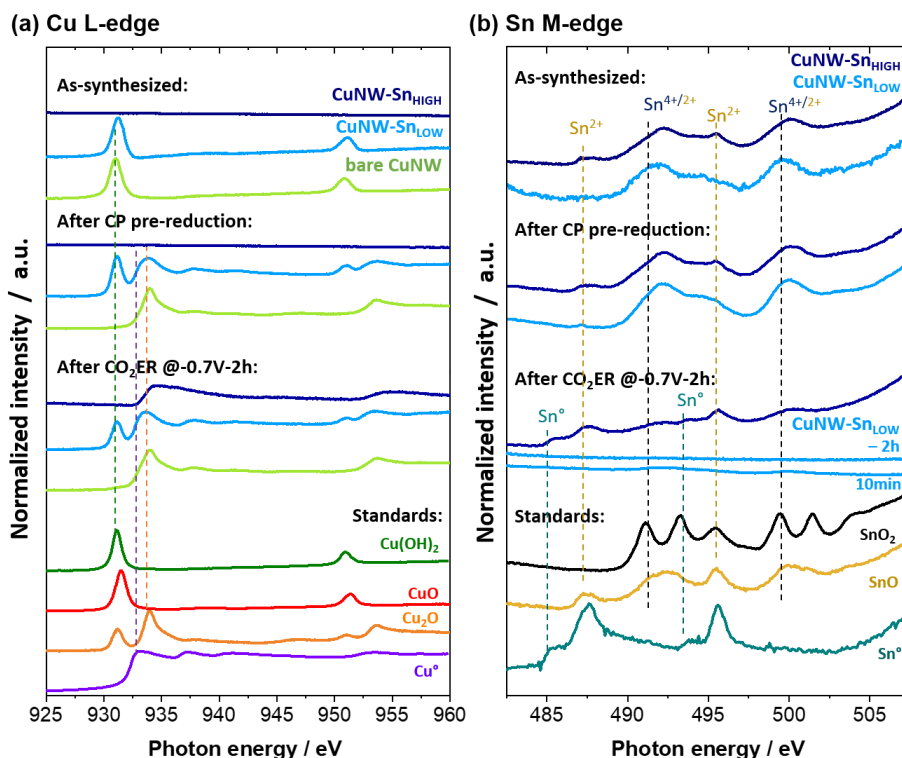
5

(a) Cu L-edge

(b) Sn M-edge

Figure 4. Ex situ soft XAS investigation of CuNW sample modified with low or high SnO_2 content. (a) Cu L-edge and (b) Sn M-edge spectra in the as-synthesized state (top), after CP pre-reduction at -2 mA cm^{-2} to -0.5 V (middle) and after CO_2ER electrolysis at -0.7 V for 2 h unless otherwise specified (bottom). Reference spectra collected from standards of metallic Cu and Sn as well are their oxides are presented, and all spectra are offset vertically to facilitate their comparison. Note that the Cu_2O reference spectrum displays a Cu^{2+} contribution (931 and 951 eV), due to surface oxidation during handling in air. Similar oxidized surface contributions are observed for Sn° and SnO.

CP pre-reduction. The results indicate that roughly the same amount of charge has been passed on all samples at the point where defined XANES Cu° features are observed; this signifies that about the same amount of Cu^{2+} has been reduced in each case, although more reductive potentials are required for reduction of samples containing Sn (Figure 3b and S2).

After CP pre-reduction until reaching a potential of -0.4 V, the samples were held at this potential for 30 min for collection of additional XANES spectra (see ESI Figure S10). However, at this stage the samples transition from self-reduction to electrocatalytic CO_2ER and HER, and bubble formation due to formation of gaseous products commences, causing disruptions to the measurement of a stable signal. To perform EXAFS data collection, a longer collection time in the post edge region is necessary, requiring a very stable signal over a duration of ca. 2.5 h per spectrum. Thus, to allow EXAFS collection, the reduction bias was decreased to -0.1 V, a potential sufficiently reducing to observe a sustained catalytic reduction current (~-150–200 µA cm^{-2}) without observable bubble-induced noise. The resulting Cu K-edge XANES spectra at -0.1 V are shown in Figure 3c; all the samples exhibit the typical features of metallic Cu° characterized by an early shoulder ~8977 eV, and all show a dominant EXAFS peak at 2.3 Å (Figure 3d) attributable to the Cu-Cu distance in metallic Cu° during CO_2ER turnover. No significant differences were observed between the XANES spectra collected at -0.4 V or -0.1 V vs RHE – for both conditions, all samples have spectra closely matching that of metallic Cu°, as shown in ESI Figure S10.

These results are in good agreement with the *ex situ* GI-XRD characterization (ESI Figure S8): after electrolysis CuNW-Sn$_{LOW}$ displays the diffraction pattern of metallic Cu°, while CuNW-Sn$_{HIGH}$ shows a mix of Cu° and Cu_6Sn_5 alloy. These observations indicate that the bulk of the CuNW samples is reduced under CO_2ER catalytic conditions and the use of hard X-rays enabled the observation of the dynamic transformation of reduction of Cu. Given the bulk sensitivity of the hard X-ray XAS measurements, the possibility of persistent surface or subsurface copper oxide reported in previous studies on pure Cu catalysts[37,38] could not be fully ruled out by this data. In order to more selectively probe the catalysts' surface, complimentary investigations by soft XAS and XPS were conducted.

Ex situ investigation of Cu L- and Sn M-Edges via soft X-ray absorption

The Cu L- and Sn M-edge XAS experiments were conducted at the LiXEdrom experimental station at the UE56/2 PGM-2 beamline at BESSY II.[39] Cu L- and Sn M-edge are investigated in the soft X-ray range (E <1000 eV) in which photons have a shallower probing depth (<100 nm in Cu)[33] as compared to the hard X-rays used above. Furthermore, when evaluated using total electron yield (TEY) detection mode, the probing depth is restricted to the mean free path of photoelectrons generated near the surface <10 nm[40,41]. While this method offers good surface sensitivity, the attenuation of soft X-rays and photoelectrons in water prevents this method from being applied *in situ* during electrocatalysis. To achieve surface-

sensitive analysis of samples resembling their catalytically-active form, we compromised by first conducting the electrochemical experiments (CP pre-reduction until -0.5 V, and electrolysis a constant potential of -0.7 V) inside an O_2-free glovebox and then transferring them directly into the high-vacuum chamber for soft XAS analysis. By this approach we sought to mitigate electrode re-oxidation in air, although a brief period of air exposure (~15-20 min) was unavoidable during the transfer step. A series of relevant standards (Cu and Sn metals and oxides) were also measured for reference (see ESI S.3.2 and Figure S11).

In the as-synthesized condition, the Cu L-edge spectra (Figure 4a) for the bare CuNW and CuNW-Sn$_{LOW}$ exhibit white line L_3 and L_2 peaks typical of $Cu(OH)_2$ (931.1, 950.9 eV) and CuO (931.4, 951.4 eV) reference spectra.[42–44] For CuNW-Sn$_{HIGH}$ (which are coated by approximately 20 nm ALD SnO_2) the Cu L-edge region is completely featureless due to blocking of Cu photoelectrons by the SnO_2 overlayer, providing evidence of both the surface sensitivity of the method and of the conformal nature of the ALD SnO_2 film. The Sn M-edge spectra (Figure 4b) of as-synthesized CuNW-Sn$_{LOW}$ and CuNW-Sn$_{HIGH}$ display signals in the expected positions for the main peaks in SnO (487.9 eV and 495.5 eV)[45,46] and SnO_2 (~492 eV and ~500 eV).[45,46] The spectra best resemble the SnO reference; however, the SnO reference spectrum is likely to display a mixture of SnO and SnO_2 features due to surface oxidation during handling in air (see ESI S.3.2 and Figure S11). On the other hand, CuNW-Sn samples composed of SnO_2 ALD layers, as confirmed by Sn 3d XPS spectra (*vide infra*), can display SnO features due radiation induced (partial) reduction of SnO_2 layer. These convoluted features of Sn^{2+} and Sn^{4+} are hereafter denoted SnO_x.

After pre-reduction to -0.5 V, the bare CuNW and CuNW-Sn$_{LOW}$ display Cu L_3, L_2 peaks at 933.9 and 953.8 eV respectively, which can be assigned to a mix of reduced Cu in Cu° or Cu^+ oxidation states.[42,43] Similar features are observed after electrolysis at -0.7 V. Interestingly, at both reduction stages (-0.5 V and -0.7 V) CuNW-Sn$_{LOW}$ displays a signal (931.1 eV) of residual Cu^{2+} which decreases at higher reductive bias. After the CuNW-Sn$_{HIGH}$ undergoes pre-reduction, it still shows no peaks in the Cu-L edge region, indicating the persistence of a Sn enriched surface, at least as thick as the probing depth (~10 nm). However, after electrolysis at -0.7 V, CuNW-Sn$_{HIGH}$ displays incipient Cu-L edge features at the positions expected for the main white lines of metallic Cu, but without any evidence of Cu^{2+}. The emergence of Cu signal in this sample coincides with the decrease in surface Sn signal observed in Sn M-edge spectra, further discussed below.

The Sn M-edge spectra (Figure 4b) reveal that the SnO_x overlayer persists unchanged after the CP pre-reduction up to -0.5 V. However, after CO_2 electrolysis at -0.7 V a decrease in Sn signal is observed for both CuNW-Sn$_{LOW}$ and CuNW-Sn$_{HIGH}$, suggesting that the surface Sn content decreases under CO_2ER conditions (possibly due to migration from surface to bulk or dissolution) to yield a surface composition differing from the as-synthesized state. This is consistent with the observations of Schreier et al.,[16] and will be discussed in more detail in the following section. In the sample with high Sn content (CuNW-Sn$_{HIGH}$) the weakened signal (Figure 4b) displays a shoulder at

~485 eV characteristic of metallic Sn°,[41] in agreement with GI-XRD characterization displaying formation of Cu_6Sn_5 alloy (ESI Figure S8), as well as the typical features of SnO.[41,45] In comparison, the sample with little Sn (CuNW-Sn$_{LOW}$) shows a significant attenuation of its SnO_x signal after just 10 min of electrolysis at -0.7 V, and after 2 h at -0.7 V no signal from Sn is observable. The question remains as to whether in this sample the Sn is present at the surface as Sn° or SnO_x but below the detection limit of this technique.

The soft X-ray absorption investigation provides insight on the surface structure and composition changes taking place the CuNW-Sn samples during CO_2 electroreduction. In all samples, surface Cu appears readily reduced from Cu^{2+} to $Cu°/Cu^+$ after the pre-reduction step to -0.5 V. On the other hand, Sn persists as a SnO_x enriched surface overlayer after the pre-reduction step. However, after electrolysis at -0.7 V, the Sn M-edge signal decreases for both samples CuNW-Sn$_{LOW}$ and CuNW-Sn$_{HIGH}$ in comparison to the as-synthesized state, indicating a significant decrease in Sn content at the near surface depth (<10 nm) probed by soft XAS, presumably due to migration from surface to bulk or dissolution. Additionally, the results indicate residual surface content of oxidized Cu as Cu^+ and Cu^{2+}, as well as SnO. Due to the brief exposure to air of the sample prior to insertion into the vacuum chamber, it is not possible to know if the observed Cu^+, Cu^{2+}, SnO surface species persist at the applied reductive bias or if they are quickly and spontaneously formed after removing the bias during sample handling. Nevertheless, the reproducible trend of Cu^{2+} signal in CuNW-Sn$_{LOW}$ sample in the different conditions tested suggests that the inclusion of low amounts of Sn may render near-surface Cu atoms more prone to oxidation. Similar trends were observed in *ex situ* surface-sensitive XPS investigations of CuSn alloys.[20,21]

Quasi in situ XPS

Ex situ soft XAS studies revealed the presence of Cu_2O, $Cu(OH)_2$ and SnO_x at the catalysts surface, as well as decrease of near-surface Sn content during CO_2ER. In order to investigate if the observed copper and tin oxidized species are the product of fast reoxidation during brief air exposure and quantify the observed decrease of surface Sn during catalytic turnover, a quasi *in situ* investigation by XPS was conducted. XPS spectra for CuNW samples with different SnO_x content (bare CuNW, CuNW-Sn$_{LOW}$ and CuNW-Sn$_{HIGH}$) were collected in as-synthesized condition as well progressive reductive conditions after CP pre-reduction to -0.5 V, after 2 h catalysis at -0.7 V, and after 2 h catalysis at -0.9 V. The electrochemical testing was conducted under inert atmosphere in a glovebox, then the samples were dried, and promptly transferred to the XPS chamber using a gastight transfer module. By this method, the exclusion of atmospheric oxygen exposure is ensured, preventing oxidation and making the resulting electrode surfaces more representative of their
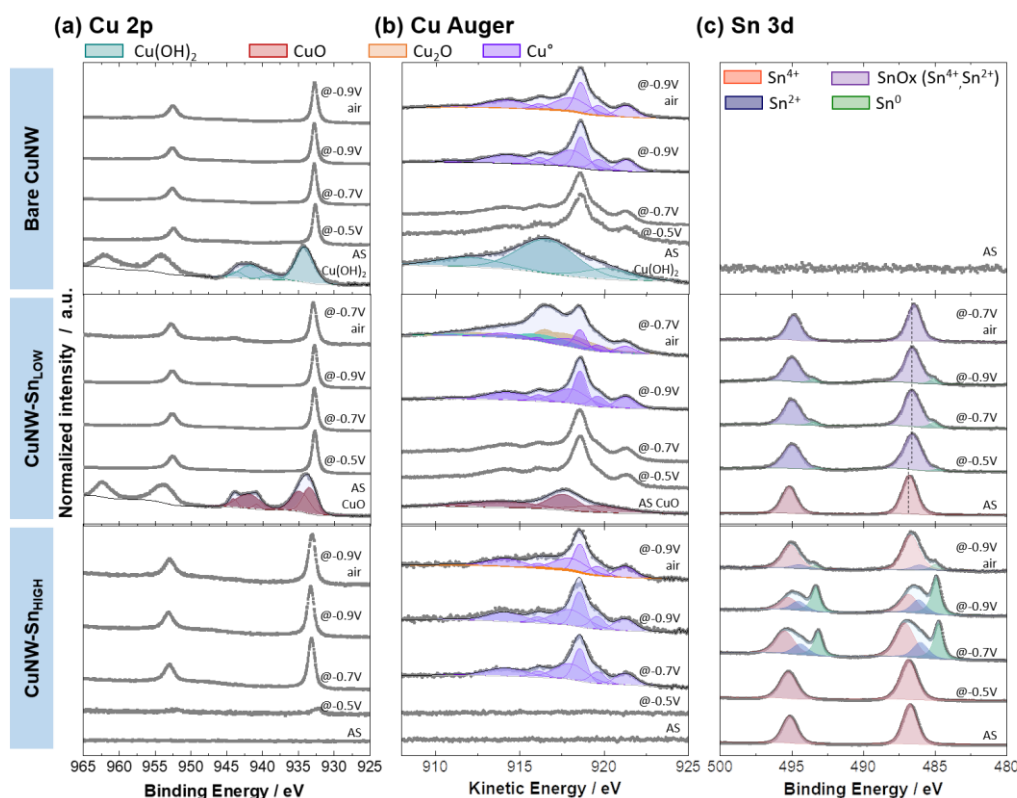
Figure 5. XPS spectra for (a) Cu 2p, (b) Cu Auger and (c) Sn 3d core levels for CuNW samples modified with different SnO_2 content (bare CuNW (top), CuNW-Sn$_{LOW}$ (middle) and CuNW-Sn$_{HIGH}$ (bottom)) in their as-synthesized (AS) state and after different electrochemical tests: after chronopotentiometry activation at -2 mA cm^{-2} up to -0.5 V, after 2 h CO_2ER electrolysis at -0.7 V and -0.9 V, and after exposure to air. Spectra are presented with a vertical offset to facilitate comparison.

active forms, while also taking advantage of the surface sensitivity of XPS.

The as-synthesized samples display the expected spectral features (Figure 5). In agreement with the XRD characterization bare CuNW displays a Cu 2p spectrum (main peak at binding energy (BE) of 933.9 eV and shake-up satellite structure) and Cu LMM Auger spectrum typical for $Cu(OH)_2$. The sample modified with a low content of Sn, CuNW-Sn$_{LOW}$, exhibits Cu 2p (main peak at BE 934.1 eV and shake-up satellite structure) and Cu LMM spectral features of CuO. For both samples, Cu 2p and Cu LMM Auger spectra can be accurately fitted with the peak model described by Biesinger[47] for $Cu(OH)_2$ and CuO (see details on peak model in ESI Section S.4.1, Table S3).

The study of progressive reduction on the bare CuNW sample indicates that the catalysts' surfaces are fully reduced to metallic Cu° after CP activation up to -0.5 V (Figure 5a,b) as indicated by the sharp Cu 2p doublet with the main peak at BE 932.7 eV, as well as the metallic Cu° Cu LMM Auger fingerprint characterized by a multiplet centered at a sharp main peak at a kinetic energy (KE) of 918.6 eV. The Cu LMM spectra can be evaluated by the peak model described by Biesinger for freshly sputtered metallic Cu surface and validated by an additional internal reference measurement of an Ar sputtered Cu foil (see details on peak model in ESI Section S.4.1, Table S2). Similar Cu 2p and Cu LMM spectra are observed for samples after CO_2 electrolysis at -0.7 V and -0.9 V, indicating that Cu is fully reduced at the surface to metallic Cu after pre-reduction up to -0.5 V and stays reduced during electrolysis at higher bias. No

evidence of residual Cu oxides on the electrode surface are detected by XPS when transferred to the analysis chamber under inert atmosphere, contrasting the above observations from ex situ soft XAS following brief air exposure, and validating the usefulness of the air-free transfer methodology.

A similar behavior was observed for Cu in CuNW-Sn$_{LOW}$ – it appears to be fully reduced to metallic Cu° after CP activation up to -0.5 V and remains reduced after CO_2 electrolysis at -0.7 V and -0.9 V (Figure 5 a-b). As observed in the soft-XAS measurements, the sample CuNW-Sn$_{HIGH}$ does not show any Cu related signals in the as-synthesized state, indicating that the SnO_2 ALD layer (~20 nm) covers all the CuNW surface (Figure 5a-b). After CP pre-reduction up to -0.5 V an incipient Cu 2p signal appears at the position expected for metallic Cu° indicating that a SnO_2 ALD layer remains enriched at the catalyst surface after the CP pre-reduction step, as previously observed by soft XAS (Figure 4b). After CO_2 electrolysis at -0.7 V and -0.9 V, typical Cu 2p and Cu LMM spectral features assigned to metallic Cu° are dominant, indicating full reduction of Cu and its migration from core to surface during CO_2ER electrolysis (Figure 5a-b).

The XPS experiments demonstrate that in all samples the Cu is readily reduced to Cu° during CP pre- reduction and remains reduced after CO_2 electrolysis at -0.7 V and -0.9 V, in agreement with bulk Cu reduction observed *in situ* by hard X-ray spectroscopy (Figure 3). The oxidation state in pure Cu catalysts during CO_2ER electrolysis has been widely investigated and remains a topic of debate.[48] Some studies have found evidence of persistence of surface or subsurface oxide[37,38,49,50] while our
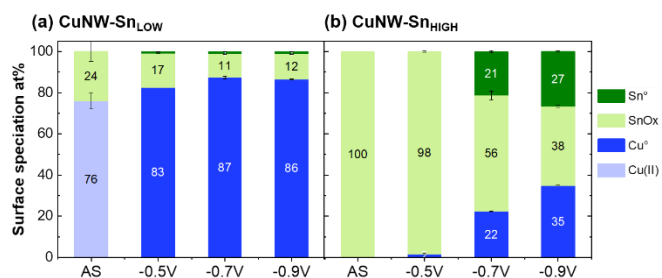
Figure 6. Surface metal speciation derived from XPS analysis, expressed as at. % of each species relative to total metal (Cu+Sn) for (a) CuNW-Sn$_{LOW}$ and (b) CuNW-Sn$_{HIGH}$.

observation of full reduction to Cu° under CO$_2$ER relevant potentials is in agreement with recent investigations performed by in situ XAS[35,51,52] and quasi in situ XPS[53] for pure Cu catalysts. In the context of a bimetallic Cu-Sn structure, it is interesting to note that the functionalization of the Cu(OH)$_2$ nanowires with SnO$_2$ does not affect their full reduction to Cu°.

The investigation of the progressive reduction of the SnO$_2$ layer by XPS (Figure 5c) indicate different Sn speciation in CO-selective (CuNW-Sn$_{LOW}$) and formate-selective (CuNW-Sn$_{HIGH}$) catalysts. In the as-synthesized state, both display a doublet with the main peak for the Sn 3d$_{5/2}$ component at BE 486.7 eV in agreement with reported value for SnO$_2$.[29,30] CuNW-Sn$_{LOW}$ exhibits a slight shift towards lower BE 486.5 eV after CP activation to -0.5 V, indicating a partial reduction to SnO (i.e. Sn^{2+}), as well as peak broadening which may indicate a mixed contribution of both Sn^{2+} and Sn^{4+} oxidation states. Due to this convolution, we denote this composition as SnO$_x$. After CO$_2$ electrolysis at -0.7 V and -0.9 V, a peak at 486.5 eV assigned to SnO$_x$ and a small shoulder at 485 eV assigned to metallic Sn° are observed (Figure 5c). The results indicate that following operation under all CO$_2$ER conditions (-0.5, -0.7 and -0.9 V), CuNW-Sn$_{LOW}$ surface is composed of fully reduced metallic Cu° and Sn predominantly in an oxidized state (Figure 5c, Figure 6a), providing experimental support for previous DFT studies which identify the persistence oxidized Sn as a crucial selectivity director in Cu-Sn CO-selective catalysts.[22,28]

For the formate-selective catalyst, CuNW-Sn$_{HIGH}$, the Sn 3d signal broadens but remains at the same position after CP pre-reduction, indicating that the SnO$_x$ ALD layer persists mostly unchanged, as observed by soft XAS (Figure 4b). Examination of electrodes after CO$_2$ electrolysis at -0.7 V and -0.9 V, the Sn 3d spectra develop new peaks assigned to Sn^{2+} (486.4 eV) and metallic Sn° (484.9 eV) (Figure 5c). Thus, after CO$_2$ electrolysis at -0.7 V and -0.9 V the CuNW-Sn$_{HIGH}$ catalyst surface is composed of metallic Cu° and a mixture of metallic Sn° and SnO$_x$ (Figure 5c and 6b). The observation of SnO$_x$ species following CO$_2$ER electrolysis in Cu-Sn formate-selective catalysts is in good agreement with previous in situ Sn L3-edge XANES[27] and Sn K-edge EXAFS[18] studies. This persistence of SnO$_x$ species must be considered when modeling Cu-Sn surfaces for mechanistic DFT investigations.

Interestingly, the potentials where Sn° emerges at the surface (-0.7 V) correspond with the potentials at which formate

selectivity begins, before reaching high selectivity of 80% at -0.9 V. In contrast, at potentials less reductive than -0.7 V where Cu°/SnO$_x$ are observed (see XPS Figure 5 and XRD ESI Figure S8), H$_2$ is the dominating product (Figure 2d). While the persistence of surface SnO$_x$ moieties has been demonstrated as beneficial for formate selectivity in pure Sn catalysts,[29–31,54] our results indicate that only when reduced metallic Sn° is formed at the catalyst surface, high formate selectivity is observed.

The surface composition and speciation are summarized in Table 1 and Figure 6. The CuNW-Sn$_{LOW}$ catalyst surface displays a Sn fraction (relative to total Cu + Sn content) of 24 at. % in the as-synthesized condition, which decreases to 19 at. % after CP activation and at ~13 at. % after electrolysis at -0.7 V and -0.9 V. This Sn content is in good agreement with surface composition reported in previous studies on low surface area CO-selective Cu-Sn catalysts[21,22,28] and Sn functionalized Cu foams.[23]

Similarly, in the formate-selective catalyst, CuNW-Sn$_{HIGH}$, originally the catalyst surface is composed of SnO$_2$ exclusively (~20 nm), which remains largely unaffected after CP pre-reduction (98 at. % Sn). However, after CO$_2$ electrolysis at -0.7 V and -0.9 V the bulk structure is reduced to Cu and the Cu$_6$Sn$_5$ alloy according to GI-XRD (ESI Figure S8), while Cu is enriched in the near surface region leading to a decrease in surface Sn content to 78 at. % and 65 at. % respectively. These results are in good agreement with the bulk composition of CuSn$_3$ reported in smooth[27] and nanostructured[18] formate-selective catalysts.

The surface Sn content decrease observed by XPS for both samples, CuNW-Sn$_{LOW}$ and CuNW-Sn$_{HIGH}$, is in agreement with the qualitative decrease observed in Sn M-edge spectra (Figure 4b). This Sn decrease is presumably due to a combined effect of Cu migration from the CuNW core to the surface during electrolysis as evidenced by the growth of Cu 2p and LMM signal observed by XPS and a partial Sn loss, as evidenced by the decrease of bulk Sn content observed by EDX and further confirmed by ICP-OES analysis of electrolyte samples (ESI Table S1).

Effects of air exposure

To investigate impact of air exposure in the surface composition of Cu-Sn bimetallic catalysts, some "post-electrolysis" samples were remeasured by XPS after intentional exposure to air for a duration of 20 min (labeled "air" in Figure 5). Minor changes are observed on the Cu 2p and Cu LMM spectra for bare CuNW and CuNW-Sn$_{HIGH}$ indicating the presence of small amounts of Cu$_2$O. However, the CuNW-Sn$_{LOW}$ sample displays growth of Cu^{2+} shake-up structure in the Cu 2p spectrum, and the Cu LMM Auger spectrum was found to be composed by a mix of Cu°, Cu$_2$O and Cu(OH)$_2$ (Figure 5a and 5b). These results are in good agreement with the observation of persistent Cu^{2+} signal in ex situ soft XAS Cu L-edge spectra (Figure 4a). The quasi in situ XPS experiments demonstrate, however, that the oxidized Cu$^+$/Cu^{2+} signals observed in the ex situ XAS study are generated during the brief period of exposure to air, which suggests that the modification of CuNW structures with low Sn content may facilitate the oxidation of Cu° in air.

Table 1. Summary of bulk and surface characterization XRD, EDX, and XPS for CuNW modified with low and high Sn content by ALD overlayers as synthesized and following CO_2 reduction at different applied potentials.

Sample description		Bulk structure XRD/Hard XAS	Sn at.%[a], [b]		Surface speciation
			Bulk (EDX)	Surface (XPS)	
CuNW-Sn$_{LOW}$	as synthesized	CuO	2.2 ± 0.3	24 ± 4.9	CuO/ SnOx
	-0.5 V	Cu°		19 ± 1.9	Cu°/SnOx
	-0.7 V	Cu°	1.5 ± 0.1	13 ± 0.7 (14 ± 0.8)[c]	Cu°/SnOx
	-0.9 V	Cu°	1.7 ± 0.1	14 ± 0.3 (14 ± 3.8)[c]	Cu°/SnOx
CuNW-Sn$_{HIGH}$	as synthesized	CuO	23 ± 1.1	100 ± 0	CuO/ SnOx
	-0.5 V	Cu°		98 ± 0.4	Cu°/SnOx
	-0.7 V	Cu°/Cu$_6$Sn$_5$	17 ± 2.6	78 ± 0.2 (82± 1.4)[c]	Cu°/Sn°/SnOx
	-0.9 V	Cu°/Cu$_6$Sn$_5$	16 ± 1.3	65 ± 0.9 (77± 2.1)[c]	Cu°/Sn°/SnOx

[a] Sn at. % relative to total metal (Cu+Sn).

[b] Sn at. % data presented as the average value ± standard deviation at 3 different sample locations.

[c] Sn at. % after intentional exposure of samples to air for 20 min

Furthermore, and most significantly, the metallic Sn° formed after CO_2 electrolysis at -0.7 V and -0.9 V is quickly re-oxidized in air, displaying spectra mostly composed by SnO$_x$ (Figure 5c bottom). Further details on the effect of air exposure are discussed in the ESI Section S.5 and Figure S12.

Interestingly, air exposure can also influence the Cu/Sn surface quantification. As an example, after CO_2ER at -0.9 V the total Sn surface content determined by XPS on the CuNW-Sn$_{HIGH}$ sample increases from 65 to 77 at. % after air exposure (Table 1), while for CuNW-Sn$_{LOW}$ under similar conditions there is no significant change in Sn content. These observations confirm that ex situ characterization of catalysts conducted "postmortem" after electrochemical testing and with air exposure can be susceptible to significant changes in surface speciation and quantification due to fast oxidation of metal surfaces in air, and migration of oxophilic metals such as Sn towards the surface upon air exposure.

The quasi *in situ* XPS results demonstrate that conducting electrochemical testing in an O$_2$-free environment and transferring the samples under inert atmosphere to the XPS analysis chamber can successfully prevent surface re-oxidation and allows one to analyze the catalyst surface as close as possible to *in situ* conditions in the absence of more sophisticated and challenging approaches such as near ambient pressure (NAP) XPS.[55–57]

Conclusions

Cu(OH)$_2$ nanowire array electrodes modified by SnO$_2$ ALD overlayers were optimized to reach high selectivity towards either CO or formate depending on the number of ALD cycles (15 or 182 cycles, respectively) with negligible differences in electrode morphology. These Cu-Sn mixed oxide composites were studied via a comprehensive investigation of metal oxidation states and chemical environments following progressive reduction of the materials during CO_2ER by bulk sensitive hard X-ray absorption spectroscopy, and surface sensitive soft X-ray absorption and XPS, in order to reach better understanding of Cu-Sn synergetic effects.

Our results indicate that Cu-Sn based CO-selective catalysts display optimal selectivity at a medium bias of -0.7 V, where their surface is composed of metallic Cu and SnO$_x$ with a Sn surface content of ~13 at %. On the other hand, formate-selective catalysts display optimal selectivity at a higher bias of -0.9 V, under these conditions their surface is composed of metallic Cu and a mixture of metallic Sn and SnO$_x$, with a Sn surface content of ~70 at.%. Further improvement of Cu-Sn catalysts performance by increasing the catalytic current density may be achieved by targeting the above mentioned surface compositions through functionalization of high surface area Cu nanostructures with Sn overlayers integrated in gas diffusion electrode configurations.[58] Such approaches can potentially enable selective and energy efficient CO or formate production at practical conversion rates using earth-abundant catalyst materials.

Overall, the complimentary information gathered by bulk and surface sensitive characterization techniques has allowed us to unravel the complex and dynamic nature of structural and compositional changes observed in Cu-Sn bimetallic electrocatalysts under CO_2ER turnover. Our findings highlight the importance of conducting thorough structural characterization by *in situ* or quasi *in situ* approaches with consideration to bulk vs surface sensitivity, and, when possible, avoiding ambient conditions (such as air exposure) which can drastically affect observed composition and speciation. *In situ* studies by hard XAS can reveal structural information under true operating conditions, but this typically requires a synchrotron and furthermore gives predominantly bulk-sensitive information. Methods which are mostly surface-sensitive (such as soft XAS and XPS) are more challenging to accomplish *in situ*, so a good compromise is to conduct electrocatalyst testing and then transfer the samples to the analysis chamber under inert atmosphere, in order to study the electrode material as close as possible to relevant catalytic conditions.

Author Contributions

Conflicts of interest

There are no conflicts to declare.

Acknowledgements

References

1   K. P. Kuhl, E. R. Cave, D. N. Abram and T. F. Jaramillo, *Energy Environ. Sci.*, 2012, **5**, 7050–7059.

2   J. B. Greenblatt, D. J. Miller, J. W. Ager, F. A. Houle and I. D. Sharp, *Joule*, 2018, **2**, 381–420.

3   S. Sen, D. Liu and G. T. R. Palmore, *ACS Catal.*, 2014, 3091–3095.

4   A. Dutta, M. Rahaman, M. Mohos, A. Zanetti and P. Broekmann, *ACS Catal.*, 2017, **7**, 5431–5437.

5   K. D. Yang, W. R. Ko, J. H. Lee, S. J. Kim, H. Lee, M. H. Lee and K. T. Nam, *Angew. Chemie - Int. Ed.*, 2017, **56**, 796–800.

6   K. Klingan, T. Kottakkat, Z. P. Jovanov, S. Jiang, C. Pasquini, F. Scholten, P. Kubella, A. Bergmann, B. Roldan Cuenya, C. Roth and H. Dau, *ChemSusChem*, 2018, **11**, 3449–3459.

7   F. S. Roberts, K. P. Kuhl and A. Nilsson, *Angew. Chemie Int. Ed.*, 2015, **54**, 5179–5182.

8   C. W. Li, J. Ciston and M. W. Kanan, *Nature*, 2014, **508**, 504–507.

9   M. Ma, K. Djanashvili and W. A. Smith, *Phys. Chem. Chem. Phys.*, 2015, **17**, 20861–20867.

10 Y. Lum, B. Yue, P. Lobaccaro, A. T. Bell and J. W. Ager, *J. Phys. Chem. C*, 2017, **121**, 14191–14203.

11 H. Mistry, A. S. Varela, C. S. Bonifacio, I. Zegkinoglou, I. Sinev, Y.-W. Choi, K. Kisslinger, E. A. Stach, J. C. Yang, P. Strasser and B. R. Cuenya, *Nat. Commun.*, 2016, **7**, 12123.

12 D. Ren, Y. Deng, A. D. Handoko, C. S. Chen, S. Malkhandi and B. S. Yeo, *ACS Catal.*, 2015, **5**, 2814–2821.

13 S. Nitopi, E. Bertheussen, S. B. Scott, X. Liu, A. K. Engstfeld, S. Horch, B. Seger, I. E. L. Stephens, K. Chan, C. Hahn, J. K. Nørskov, T. F. Jaramillo and I. Chorkendorff, *Chem. Rev.*, 2019, **119**, 7610–7672.

14 A. Vasileff, C. Xu, Y. Jiao, Y. Zheng and S. Z. Qiao, *Chem*, 2018, 1–23.

15 M. K. Birhanu, M. C. Tsai, A. W. Kahsay, C. T. Chen, T. S. Zeleke, K. B. Ibrahim, C. J. Huang, W. N. Su and B. J. Hwang, *Adv. Mater. Interfaces*, 2018, **5**, 1–34.

16 M. Schreier, F. Héroguel, L. Steier, S. Ahmad, J. S. Luterbacher, M. T. Mayer, J. Luo and M. Grätzel, *Nat. Energy*, 2017, **2**, 17087.

17 S. Sarfraz, A. T. Garcia-Esparza, A. Jedidi, L. Cavallo and K. Takanabe, *ACS Catal.*, 2016, **6**, 2842–2851.

18 K. Ye, Z. Zhou, J. Shao, L. Lin, D. Gao, N. Ta, R. Si, G. Wang and X. Bao, *Angew. Chemie - Int. Ed.*, 2020, **59**, 4814–4821.

19 X. Hou, Y. Cai, D. Zhang, L. Li, X. Zhang, Z. Zhu, L. Peng, Y. Liu and J. Qiao, *J. Mater. Chem. A*, 2019, **7**, 3197–3205.

20 A. Vasileff, C. Xu, L. Ge, Y. Zheng and S. Z. Qiao, *Chem. Commun.*, 2018, **54**, 13965–13968.

21 M. Morimoto, Y. Takatsuji, R. Yamasaki, H. Hashimoto, I. Nakata, T. Sakakura and T. Haruyama, *Electrocatalysis*, 2018, **9**, 323–332.

22 Q. Li, J. Fu, W. Zhu, Z. Chen, B. Shen, L. Wu, Z. Xi, T. Wang, G. Lu, J. J. Zhu and S. Sun, *J. Am. Chem. Soc.*, 2017, **139**, 4290–4293.

23 J. Zeng, K. Bejtka, W. Ju, M. Castellino, A. Chiodoni, A. Sacco, M. A. Farkhondehfal, S. Hernández, D. Rentsch, C. Battaglia and C. F. Pirri, *Appl. Catal. B Environ.*, 2018, **236**, 475–482.

24 W. Ju, J. Zeng, K. Bejtka, H. Ma, D. Rentsch, M. Castellino, A. Sacco, C. F. Pirri and C. Battaglia, *ACS Appl. Energy Mater.*, 2019, **2**, 867–872.

25 Y. Zhao, C. Wang and G. G. Wallace, *J. Mater. Chem. A*, 2016, **4**, 10710–10718.

26 C. Chen, Y. Pang, F. Zhang, J. Zhong, B. Zhang and Z. Cheng, *J. Mater. Chem. A*, 2018, **6**, 19621–19630.

27 X. Zheng, Y. Ji, J. Tang, J. Wang, B. Liu, H. G. Steinrück, K. Lim, Y. Li, M. F. Toney, K. Chan and Y. Cui, *Nat. Catal.*, 2019, **2**, 55–61.

28 A. Vasileff, X. Zhi, C. Xu, L. Ge, Y. Jiao, Y. Zheng and S. Z. Qiao, *ACS Catal.*, 2019, **9**, 9411–9417.

29 Y. Chen and M. W. Kanan, *J. Am. Chem. Soc.*, 2012, **134**, 1986–9.

30 S. Zhang, P. Kang and T. J. Meyer, *J. Am. Chem. Soc.*, 2014, **136**, 1734–7.

31 D. H. Won, C. H. Choi, J. Chung, M. W. Chung, E. H. Kim and S. I. Woo, *ChemSusChem*, 2015, **8**, 3092–3098.

32 Helmholtz-Zentrum Berlin für Materialen und Energie, *J. large-scale Res. Facil.*, 2016, **2**, A49.

33 B. L. Henke, E. M. Gullikson and J. C. Davis, *At. Data Nucl. Data Tables*, 1993, 54, 181–342.

34 G. S. Henderson, F. M. F. de Groot and B. J. A. Moulton, *Rev. Mineral. Geochemistry*, 2014, **78**, 75–138.

35 S. H. Lee, J. C. Lin, M. Farmand, A. T. Landers, J. T. Feaster, J. E. Avilés Acosta, J. W. Beeman, Y. Ye, J. Yano, A. Mehta, R. C. Davis, T. F. Jaramillo, C. Hahn and W. S. Drisdell, *J. Am. Chem. Soc.*, 2021, **143**, 588–592.

36 M. Farmand, A. T. Landers, J. C. Lin, J. T. Feaster, J. W. Beeman, Y. Ye, E. L. Clark, D. Higgins, J. Yano, R. C. Davis, A. Mehta, T. F. Jaramillo, C. Hahn and W. S. Drisdell, *Phys. Chem. Chem. Phys.*, 2019, **21**, 5402–5408.

37 F. Cavalca, R. Ferragut, S. Aghion, A. Eilert, O. Diaz-Morales, C.

Liu, A. L. Koh, T. W. Hansen, L. G. M. Pettersson and A. Nilsson, *J. Phys. Chem. C*, 2017, **121**, 25003–25009.

38 A. Eilert, F. Cavalca, F. S. Roberts, J. Osterwalder, C. Liu, M. Favaro, E. J. Crumlin, H. Ogasawara, D. Friebel, L. G. M. Pettersson and A. Nilsson, *J. Phys. Chem. Lett.*, 2017, **8**, 285–290.

39 Helmholtz-Zentrum Berlin für Materialen und Energie, *J. large-scale Res. Facil.*, 2016, **2**, A80.

40 M. Abbate, J. B. Goedkoop, F. M. F. de Groot, M. Grioni, J. C. Fuggle, S. Hofmann, H. Petersen and M. Sacchi, *Surf. Interface Anal.*, 1992, **18**, 65–69.

41 R. Qiao, I. T. Lucas, A. Karim, J. Syzdek, X. Liu, W. Chen, K. Persson, R. Kostecki and W. Yang, *Adv. Mater. Interfaces*, 2014, **1**, 1–6.

42 H. M. Hollmark, P. G. Keech, J. R. Vegelius, L. Werme and L. C. Duda, *Corros. Sci.*, 2012, **54**, 85–89.

43 P. Jiang, D. Prendergast, F. Borondics, S. Porsgaard, L. Giovanetti, E. Pach, J. Newberg, H. Bluhm, F. Besenbacher and M. Salmeron, *J. Chem. Phys.*, 2013, **138**, 024704.

44 K. I. Shimizu, H. Maeshima, H. Yoshida, A. Satsuma and T. Hattori, *Phys. Chem. Chem. Phys.*, 2001, **3**, 862–866.

45 V. Sharma, R. Vyas, P. Bazylewski, G. S. Chang, K. Asokan and K. Sachdev, *RSC Adv.*, 2016, **6**, 29135–29141.

46 A. V. Shaposhnik, D. A. Shaposhnik, S. Y. Turishchev, O. A. Chuvenkova, S. V. Ryabtsev, A. A. Vasiliev, X. Vilanova, F. Hernandez-Ramirez and J. R. Morante, *Beilstein J. Nanotechnol.*, 2019, **10**, 1380–1390.

47 M. C. Biesinger, *Surf. Interface Anal.*, 2017, **49**, 1325–1334.

48 Z.-Z. Wu, F.-Y. Gao and M.-R. Gao, *Energy Environ. Sci.*, 2021, **14**, 1121–1139.

49 M. Favaro, H. Xiao, T. Cheng, W. A. Goddard, J. Yano and E. J. Crumlin, *Pnas*, 2017, **114**, 6706–6711.

50 Y. Zhao, X. Chang, A. S. Malkani, X. Yang, L. Thompson, F. Jiao and B. Xu, *J. Am. Chem. Soc.*, 2020, **142**, 9735–9743.

51 N. J. Firet, T. Burdyny, N. T. Nesbitt, S. Chandrashekar, A. Longo and W. A. Smith, *Catal. Sci. Technol.*, 2020, **10**, 5870–5885.

52 J. J. Velasco-Velez, J. J. Velasco-Velez, R. V. Mom, L. E. Sandoval-Diaz, L. J. Falling, C. H. Chuang, D. Gao, D. Gao, T. E. Jones, Q. Zhu, Q. Zhu, R. Arrigo, B. Roldan Cuenya, A. Knop-Gericke, A. Knop-Gericke, T. Lunkenbein, R. Schlögl and R. Schlögl, *ACS Energy Lett.*, 2020, **5**, 2106–2111.

53 R. M. Arán-Ais, F. Scholten, S. Kunze, R. Rizo and B. Roldan Cuenya, *Nat. Energy*, 2020, **5**, 317–325.

54 M. F. Baruch, J. E. Pander, J. L. White and A. B. Bocarsly, *ACS Catal.*, 2015, **5**, 3148–3156.

55 A. Knop-Gericke, V. Pfeifer, J. J. Velasco-Velez, T. Jones, R. Arrigo, M. Hävecker and R. Schlögl, *J. Electron Spectros. Relat. Phenomena*, 2017, **221**, 10–17.

56 M. Salmeron, *Top. Catal.*, 2018, **61**, 2044–2051.

57 M. Favaro, F. Abdi, E. Crumlin, Z. Liu, R. van de Krol and D. Starr, *Surfaces*, 2019, **2**, 78–99.

58 B. H. Frazer, B. Gilbert, B. R. Sonдеregger and G. De Stasio, *Surf. Sci.*, **537**, 161–167.